Research Article | Vol. 29, No. 3 / 1 February 2021 / Optics Express 3438
Optics EXPRESS

FleXCT: a flexible X-ray CT scanner with 10 degrees of freedom

BJÖRN DE SAMBER, JENS RENDERS, TIM ELBERFELD, YVES MARIS, JONATHAN SANCTORUM, NATHANAËL SIX, ZHIHUA LIANG, JAN DE BEENHOUWER, AND JAN SIJBERS*

imec-Visionlab, University of Antwerp, Belgium
**Jan.Sijbers@UAntwerpen.be*

Abstract: Laboratory based X-ray micro-CT is a non-destructive testing method that enables three dimensional visualization and analysis of the internal and external morphology of samples. Although a wide variety of commercial scanners exist, most of them are limited in the number of degrees of freedom to position the source and detector with respect to the object to be scanned. Hence, they are less suited for industrial X-ray imaging settings that require advanced scanning modes, such as laminography, conveyor belt scanning, or time-resolved imaging (4DCT). We introduce a new X-ray scanner FleXCT that consists of a total of ten motorized axes, which allow a wide range of non-standard XCT scans such as tiled and off-centre scans, laminography, helical tomography, conveyor belt, dynamic zooming, and X-ray phase contrast imaging. Additionally, a new software tool 'FlexRayTools' was created that enables reconstruction of non-standard XCT projection data of the FleXCT instrument using the ASTRA Toolbox, a highly efficient and open source set of tools for tomographic projection and reconstruction.

1. Introduction

The interior of an object can be visualized with X-ray computed tomography (XCT) by acquiring X-ray radiographs of that object and reconstructing a 3D image from that set of radiographs. A conventional way of scanning is to position the object on a rotation stage that is placed between a static X-ray source and detector and subsequently rotate the object while acquiring radiographs. Hence, it is not surprising that the vast majority of commercial tomographic X-ray systems have been designed to perform circular cone-beam scans, with (only) two degrees of freedom: a rotation stage and a linear translation thereof towards the detector for zooming [see Fig. 1(a)].

While circular cone beam scanning is a convenient and widely employed scanning method, it requires the acquisition of hundreds of radiographs, equi-angularly distributed over 360 degrees. Hence, it is a time consuming acquisition technique and is often too restrictive in terms of acquisition geometry to be applicable in industrial settings. For example, plate-shaped objects can only be rotated over a limited angular range, large objects often require 'panning' movements of X-ray tube and/or detector to be imaged entirely, a conveyor belt is often the preferred method for fast quality control etc. Recently, innovative scanning systems have been developed to address such challenges by implementation of additional motors [1,2] and even robotic arms [3,4]. In this manuscript, we introduce the FleXCT system that is capable of addressing the need for versatile X-ray scanning. The FleXCT system consists of a customized UniTOMXL scanner from Tescan XRE [5] with additional degrees of freedom of movement and larger associated travel range. In total, it possesses ten motorized axes which provide independent movement of sample, detector and X-ray tube, allowing a wide range of different scanning geometries which can handle these specific needs [6].

#409982 https://doi.org/10.1364/OE.409982
Journal © 2021 Received 17 Sep 2020; revised 2 Dec 2020; accepted 7 Dec 2020; published 21 Jan 2021

Optics EXPRESS

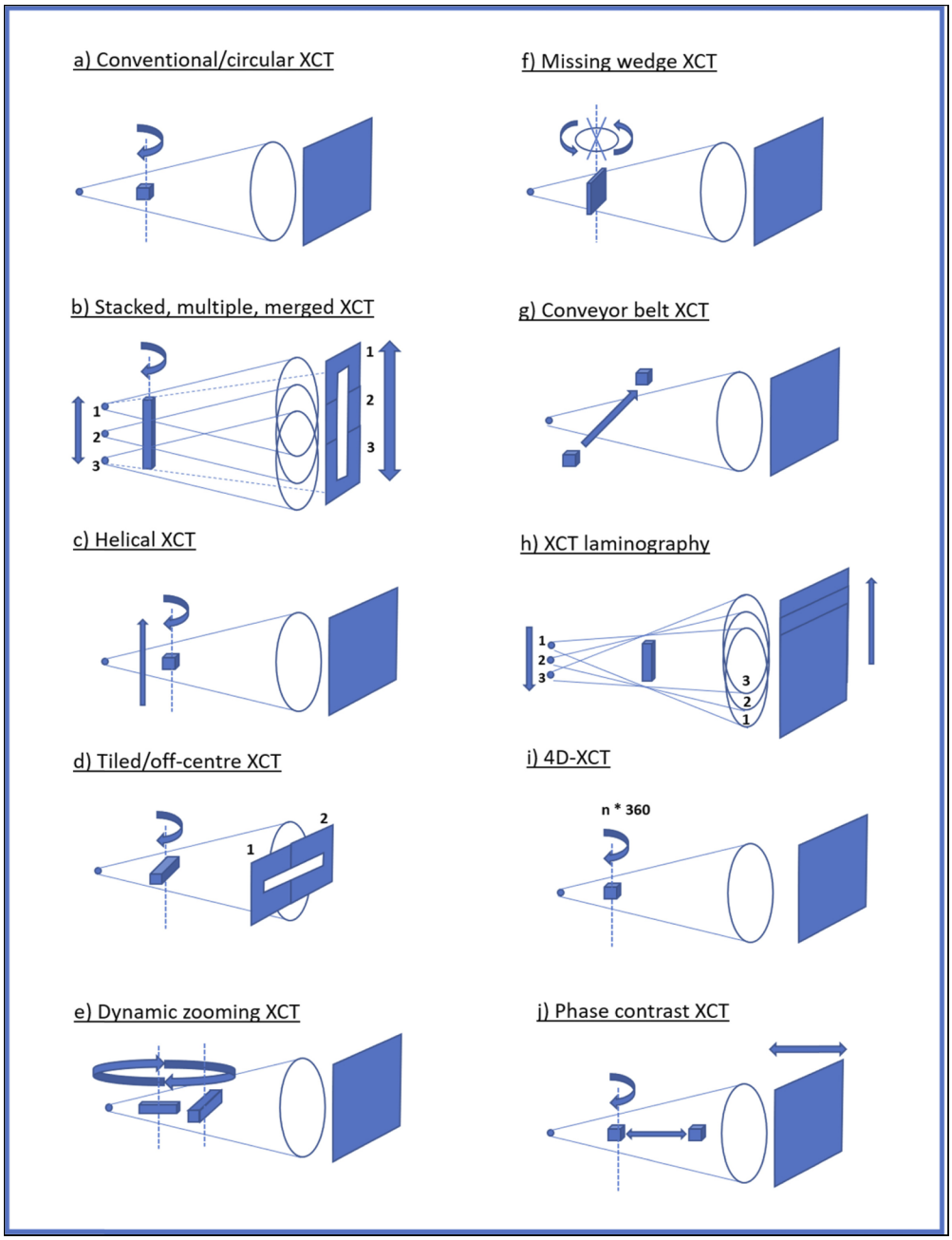

Fig. 1. Different scanning geometries achievable with the FleXCT scanner.

Optics EXPRESS

Figures 1(b)–1(i) provide an overview of non-standard scanning schemes that become possible with the FleXCT system. When high resolution imaging of the object is required of an object that cannot be entirely covered by the X-ray cone beam and/or the field-of-view of the detector, a number of partial XCT scans can be acquired instead. This can be achieved by performing XCT scans at successive, partially overlapping heights of the sample, requiring a simultaneous vertical movement of source and detector, as shown in Fig. 1(b). Helical XCT scanning [Fig. 1(c)] can be considered as a continuous mode thereof [7,8], but requires a vertical translation of the object while the object (or the entirety of source and detector) rotates. When the object of interest is too wide to be imaged completely by the detector and cannot be put upright for vertical scanning, a XCT scan with partially overlapping horizontal positions of the detector can be made. Such a 'tiled' approach requires horizontal movement of the detector panel, as shown in Fig. 1(d). In adaptive/dynamic zooming XCT [Fig. 1(e)], the source-object-distance (SOD) is changed during sample rotation, such that the object is optimally covering the detector area for every rotation angle of the sample [9,10]. In this case, movement of the sample along the source-detector axis during rotation (dynamic zooming) is required. In essence, the aforementioned scanning schemes presented in Figs. 1(b)–1(e) enable higher resolution imaging of the object compared to the conventional, circular CT scan [Fig. 1(a)]. In some cases, information of an object changing in time is desired, such as a sample undergoing a deformation [11] or a chemical reaction [12]. For such studies, four-dimensional XCT (4D XCT) experiments can be performed [Fig. 1(i)], where the sample undergoes multiple successive rotations while radiographs are being acquired. Note that 4D XCT experiments often require a specific sample environment (e.g., pressure cell, oven, . . .) and therefore a flexible positioning of source, sample stage and/or detector. Besides X-ray absorption based XCT scans, X-ray phase contrast imaging is another modality that requires geometric flexibility in the scanner: by increasing the distance between sample and detector, phase effects can be enhanced because of the longer propagation distance, which allows to distinguish materials with only slight differences in mean atomic number [Fig. 1(j)]. Phase contrast tomography can then be achieved using phase retrieval algorithms such as the Bronnikov algorithm [13] or Paganin filter [14,15].

In certain cases, rotation of the object of interest is impractical, e.g. in case of plate-type structures or large samples in general (e.g., paintings, wind or helicopter blades) [16,17]. In X-ray laminography experiments, X-ray source and detector can be moved synchronously in opposite directions along a circular path (rotational laminography) or can be translated in opposite directions [translational laminography, Fig. 1(h)], while the object remains fixed in space. Due to the correlated motion of source and detector, the location of the projected images of points within the object moves. However, points from a particular plane will always be projected at the same location onto the detector and therefore imaged sharply. All other structures of the object above and below the focal plane will be projected during the movement at different locations on the detector and therefore be superimposed as a background intensity to the focal plane when summing all the acquired radiographs, also referred to as tomosynthesis [18]. Instead of summation of all acquired projections, this focal plane can also be directly determined using a technique referred to as computed laminography (CL). For industrial in-line inspection and quality control, speed of the analysis is often paramount [19]. Therefore, conveyor belt scanning is an often preferred geometry: objects pass in a linear trajectory through the X-ray cone beam as shown in Fig. 1(g). Radiographs from a limited range of consecutive angles of the sample are obtained, which allows partial reconstruction of the object and even tomosynthesis-like reconstruction in a plane parallel to the detector. For this reason, conveyor belt scanning has also been referred to as computed laminography (CL) [20]. Additionally, a priori information of the object (e.g., a CAD model) can be added, improving the quality of the reconstruction [21]. Note that for conveyor belt scanning, a cone beam X-ray geometry is essential since a parallel X-ray beam geometry cannot be used as it does not provide a varying angular view of the sample. Additionally, a rotational

Optics EXPRESS

motion of the object can be added to the linear conveyor belt movement, which further expands the angular range of the sample probed and reconstruction quality. For laboratory investigations, the conveyor belt geometry can be mimicked by simultaneous horizontal or vertical movement of detector and source, while keeping the object fixed (or adding on the spot rotation). Another type of XCT scan belonging to this category is the so-called missing wedge CT scan [see Fig. 1(f)], where a wedge of the angular range cannot be acquired (or is of lower quality). The reason for this is, for example, a strong absorption of the sample in a certain direction or the presence of a sample environment for 4DCT experiments that blocks the X-rays in a certain angular range. In summary, versatile research X-ray scanners and accompanying reconstruction techniques are needed in order to test and optimize new techniques with non-standard geometries. This is especially true, to further the popularization of lesser known, but promising (fast) scanning and reconstruction schemes.

In order to reconstruct X-ray CT data, both analytical and iterative reconstruction methods can be employed. Due to their overall speed, analytical methods such as filtered back projection (FBP) and FDK (Feldkamp, Davis and Kress) reconstruction methods are generally used for reconstruction of highly sampled circular X-ray CT datasets [22]. On the other hand, for CT reconstruction of XCT datasets with limited data, iterative reconstruction methods become more advantageous as they allow reconstruction of the object without the need for a customized analytical solution for every non-standard geometry. Additionally, prior knowledge of the object can be included in iterative reconstructions. This prior knowledge may constitute certain physical properties such as elemental composition or geometrical properties such as information from a CAD model [21]. A large variety of iterative reconstruction techniques is currently available (e.g., SIRT, MLEM, DART, TVMIN) that are ideally suited for reconstruction of X-ray datasets with limited data. Meritorious efforts have also been made to strive towards close interaction schemes between CT scanner hardware and reconstruction software that can enable on-the-fly analysis of arbitrary slices or zooming in during live reconstruction [2]. An interesting development is the use of artificial intelligence (AI) based techniques for CT reconstruction with limited data [23,24]. To make these techniques accessible to the general public, the gap between low level tomographic reconstruction packages and high-level distributed systems must be bridged by tomographic reconstruction pipelines [25].

In this manuscript, we discuss both hardware (X-ray tube, detector, motor stages) and software (acquisition and reconstruction) aspects of the FleXCT system. The scanner's ability to perform a wide variety of unique scanning geometries, e.g. helical scanning, 4DCT, conveyor belt, dynamic zooming, laminography etc. is highlighted. In order to reconstruct non-standard XCT scans performed with the FleXCT scanner, the software package ASTRA is used [6]. Specific routines for processing non-standard XCT scans with the ASTRA Toolbox form the backbone of the in-house written Python package FlexRayTools, as such establishing the link between data from the FleXCT scanner and high quality reconstructed datasets.

2. Experimental setup

2.1. Hardware

2.1.1. X-ray tube

A schematic depiction of the FleXCT motors and a number of photographs of the main components are provided in Figs. 2(a)–2(d). The heart of the FleXCT scanner is an X-ray tube from X-ray WorX (see Table 1 for specifications). The X-ray tube covers a wide energy range from 20 to 230 keV, which can be used for imaging materials with both low (e.g., biological, polymer samples) and high mean atomic number elements (e.g., concrete and steel). In front of the X-ray tube window, a slot is present that allows insertion of different filters to pre-harden the X-ray beam, resulting in decreased cupping effects in the XCT data. Depending on the X-ray energy, different

Optics EXPRESS

filter materials and thicknesses are available: aluminum (Al, 1–1.5mm), copper (Cu, 1–1.5 mm) and tin (Sn, 0.75–1 mm). Power output of the X-ray tube is automatically adapted to the voltage using the 'autofunction' tool: the X-ray tube maximal power behaves linearly with the voltage in the range of 20–120 kV and then remains constant at 300 W starting from 120 kV. The spot size on the target from which the X-rays are produced expressed in micrometer, is approximately equal to the output power of the tube expressed in watt.

The minimal two-dimensional (2D) spatial resolution of the X-ray WorX tube, requiring a minimal power of 15 W, was determined to be 2 µm using the 'RT-RC-02' micro-chart from JIMA (Japan Inspection Instruments Manufacturers' Association). The JIMA micro-chart is made of tungsten line patterns on a 60 µm thick silicon base. The minimal three-dimensional (3D) achievable spatial resolution of the FleXCT scanner, on the other hand, was determined using a Micro-CT-Barpattern-NANO from QRM (Quality Assurance in Radiology and Medicine, Germany) of which the results are provided in Visualization 1. The Barpattern NANO phantom consists of two silicon chips that exhibit several line and point patterns representing lines and points of 1 to 15 µm. In Visualization 1, the vertical lines with a line thickness of 2 µm are still clearly visible, while for the horizontal lines this is only the case starting from 3–4 µm line thickness (indicated with a red rectangle). Using these measurements from Tescan XRE, the minimum spatial resolution of the system for the Barpattern NANO was determined to be 2 µm horizontally by 4 µm vertically (experimental conditions: 80 kV, 15W, 1.54 µm voxel size, SOD 9 mm, SDD 969 mm, 2200 projections, 2×2000 ms exposure time).

2.1.2. Detector panel

Detection of X-rays is achieved via an industrial flat panel X-ray detector (VAREX imaging, Salt Lake City, US) [26]. The detector panel is composed of a carbon fibre entrance window, single substrate amorphous silicon active TFT-diode array with a directly deposited Gd_2O_2S:Tb (Gadox) layer. The total field of view (FOV) of the detector is 2856×2856 pixels (150 µm pitch, referred to as 3K mode) and the detector has various other FOV that allow faster data-acquisition or limiting the amount of data acquired. For standard CT scans, a FOV of 1920×1896 pixel is used (also referred to as '2K' mode). The detector can be operated with exposure times ranging between 10 ms to 5000 ms and with variable capacity (LOW/HIGH gain mode). Using the total FOV and highest resolution (150 µm), 15 frames per second (fps) can be read out (67 ms exposure), increasing to 30 fps (33 ms) for binning mode 2 (300 µm panel resolution). Frame rates up to 100 fps can be obtained with a cropped field of view of 432 mm x 72 mm and binning, suited for dynamic/4DCT scans.

2.1.3. Motor stages

Since the sample stage cannot be moved in height, both X-ray tube and detector panel can be moved up and down simultaneously (in Z-direction, cf. motor axis no. 1 and 3 in Fig. 2) in order to acquire flat field images or to perform scans on larger objects (e.g. helical, STAMINA scans, see next section). More detailed information on the travel ranges of the motors is provided in Table 1. The sample motor stack comprises a high precision rotation stage (motor axis no. 8 in Fig. 2) for CT scans, with on top an XY stage [motor axis no. 9–10 in Fig. 2(d)] for centering a predefined volume of interest (VOI). The rotation stage is additionally fitted with a slip ring, so that it is not limited to a 0–360 degrees movement, but can continue rotating (e.g., for dynamic/4DCT scans).

The sample and detector stage can additionally be moved along the 2 m long optical axis (X-direction, resp. motor axis no. 7 and 5 in Fig. 2) to adjust the magnification and effective X-ray flux. Additionally, both X-ray tube, sample stage and detector panel can move laterally [i.e. in Y-direction, cf. axis no. 2, no. 6 and no. 4 in Fig. 2(d), respectively]. Lateral movement of the detector/X-ray tube enables 1) placing the vertical pixel row of the detector in the center

Optics EXPRESS

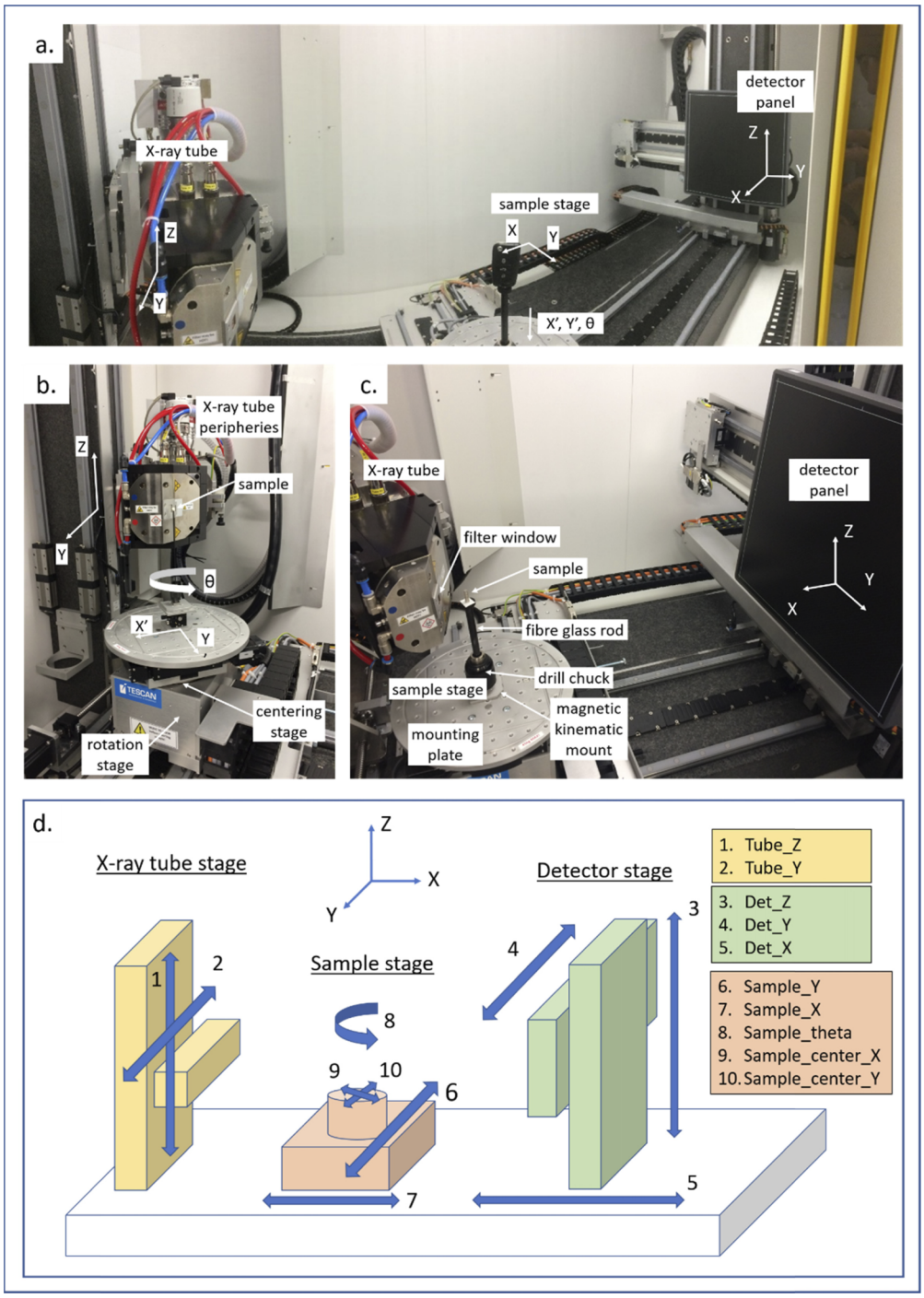

Fig. 2. a) panoramic photograph of the inside of the FleXCT scanner showing the detector panel positioned at a maximal distance of 2 m from the X-ray source, b) close-up photograph of the X-ray tube and sample stage, c) close-up photograph of X-ray tube, sample stage and detector screen at 600 mm from the X-ray source), d) Schematic drawing of FleXCT scanner showing different degrees of freedom of motor movement.

Optics EXPRESS

Table 1. Characteristics of the FleXCT scanner.

Motor Stage		
Type	Travel range	Tolerances
•Sample rotation stage (θ) – axis no. 8	limitless (due to slip ring)	axial and radial run-out at 15 cm < 1 µm
•Sample centering (XY) – axis no. 9-10	70 mm	resolution < 1 µm
•Sample translation		
○ X (along beam) – axis no. 7	2000 mm	resolution < 1 µm
○ Y (left-right) - axis no. 6	470 mm	
○ Z (height) – axis 1 + 3	880 mm	
• X-ray tube translation range		
○ Y (horizontal) – axis no. 1	240 mm	resolution < 1 µm
○ Z (vertical) – axis no. 2	900 mm	
• Detector translation range		
○ X (along beam) – axis no. 5	350-2000 mm	resolution < 1 µm
○ Y (horizontal) – axis no. 4	620 mm	
○ Z (vertical) – axis no. 3	900 mm	
X-ray tube		
Energy range	20-230 keV	
Type	open type reflection tube	
Target material	Tungsten	
Min. focus-object-distance	4 mm	
Opening angle	60°	
2D minimal resolution (based on JIMA micro-chart)	2 µm	
Power output	15 W (required for optimal resolution) up to 300W	
Flat panel X-ray detector		
panel	Single substrate radiation hard amorphous silicon TFT-diode array	
Scintillator	Gd_2O_2S:Tb (Gadox)	
Dimensions	430 × 430 mm FOV	
No. of pixels	2856 × 2856 active pixels	
Pixel size	150 µm pixel size	
Sample limitations		
• weight	80 kg when only using sample rotation stage 45 kg when also using XY stage	
• dimensions (diam. X height)	600 mm x 1150 mm	
Overall scanner properties		
3D minimal resolution (based on QRM MicroCT Bar Pattern NANO)	2 µm (hor.) x 4 µm (vert.)	
dimensions	1.58 × 3.5 × 2.1 m (WxLxH)	
weight	6500 kg	

Optics EXPRESS

of rotation and 2) performing tiled CT scans [Fig. 1(d)] for samples which are too wide to fit entirely in the detector area (and which cannot be put vertically). Sideways movement of the sample (motor axis no. 6) is typically used to: 1) bring the sample stage closer to the scanner door to ease sample mounting or 2) for conveyor belt type scanning experiments [Fig. 1(f)]. Simultaneous, but opposite sideways Y (or vertical Z) movement of X-ray tube and detector can be used for X-ray laminography scans [Fig. 1(h)].

The FleXCT scanner can also be upgraded with new hardware components, such as a second detector panel on the additional detector stage or complex setups on top of the rotation stage. For the latter, a serial interface DB15 is available on top of the rotation stage for communication with experimental sample environments (without rotation restrictions due to presence of a slip ring). The DB15 interface is connected with radiation safe cable in- and outlets to an interface panel on the external housing (IO ports, RJ45, AC/DC power).

2.2. Software

2.2.1. Acquisition

To control the FleXCT scanner, the 'Acquila' operating software package is used, a generic platform developed by Tescan in the graphical programming environment LabVIEW [27]. The software allows warm-up and setting of tube energy and power, movements of motor stages, camera view ('live' grab or snap mode), selection of a volume-of-interest (VOI) for scanning, adapt detector settings (binning, exposure, no. of replicates) and script preparation for various scan types: smooth/circular scan, step-and-shoot (discrete variant of smooth scanning), STAMINA, helical, dynamic scanning. A scripting module is available for acquiring non-standard scans such as linear (conveyor belt type) scans and laminography.

2.2.2. Reconstruction

The Acquila reconstruction software package provides a reconstruction workflow comprised of several steps: 1) normalisation (dark field subtraction and flat field division), optional (pre)ring artefact correction and/or spot filter), 2) sub-pixel determination of the centre of rotation (COR), 3) optional beam hardening correction, 4) optional phase/scatter correction, 5) adjustment offset angle and ROI selection 5) GPU aided XCT using FDK algorithm.

A standard XCT scan (2K detector mode, no cropping) can be reconstructed in approx. 10 minutes. After initial processing, additional post-processing tools are available, such as beam hardening correction, ring filter correction, batch reconstruction of XCT scans, stitching/reconstruction of tiled and STAMINA scans, dynamic data reconstruction (4DCT) and phase retrieval (e.g., Paganin, Bronnikov).

For reconstruction of non-standard XCT scans with the FleXCT scanner such as helical CT, conveyor belt, dynamic zooming and laminography, a software package called FlexRayTools was developed in-house. FlexRayTools extends the ASTRA Toolbox, an open-source software package for the development of iterative reconstruction methods for arbitrary scanning geometries [6,28–30], by adding a user-friendly interface for (scanning-) geometry definition and several iterative reconstruction methods. Arbitrary positioning of the source and detector, which is a requirement for reconstruction of non-standard scans. Additionally, composite datasets such as succeeding CT scans with different geometry of the same object are enabled.

3. Results and discussion

3.1. Stacked and tiled XCT scanning modes, providing higher spatial resolution for larger and/or asymmetrical samples

One of the limitations of conventional X-ray micro-CT is that relatively large (centimeter-sized) objects must be placed far enough from the source to fit completely into the X-ray cone beam

Optics EXPRESS

and cover the entire detector area. As a result, compared to smaller (millimeter-sized) objects that can be placed close to the source, a similar resolution cannot be reached for larger objects (or objects with a large aspect ratio). One of the approaches to enable high resolution CT on larger or asymmetric objects with the FleXCT scanner is to split up a single XCT scan vertically into consecutive, overlapping scans [see Fig. 1(b)]. In what follows, this approach is also referred to as STAMINA (Stacked, Multiple and Merged Acquisition). In order to illustrate the advantage of such stacked scanning mode, an AA alkaline battery was selected because of its large aspect ratio. The left side of Fig. 3(a) shows a schematic depiction of the battery which was first positioned within the entire field-of-view (FOV) of the detector panel and the resulting reconstructed cross section on the right. The zoom factor is limited by the height of the object, providing a minimal voxel size of 33 µm in this case. Figure 3(b) shows a schematic depiction of the STAMINA scan performed and the resulting cross section. Here, five CT scans are acquired of the battery that partially overlap in the vertical direction by vertically moving the source and detector by 11.636 mm after each scan. More details on the experimental settings of both scans are provided in Table 2. After acquisition, virtual cross sections obtained by the STAMINA method were reconstructed in batch procedure using FDK back projection for each individual scan (reconstruction parameters such as centre of rotation (COR), beam hardening correction (BHC) were kept constant). Afterwards, overlap between the different batches of reconstructed cross-sections is identified and discarded, after which the final image stack is obtained. Using the latter scanning procedure resolution could be improved down to 8 µm, clearly providing more detail of the inside morphology of the battery. Note that STAMINA has the advantage that long objects can be placed up straight for scanning, causing less absorption effects. Additionally, due to the large translation range of the source and detector of the FleXCT, objects up to 1 m high can be scanned using this method.

In addition to stacked scanning along the vertical direction (STAMINA), the horizontal field of view of the detector can also be enlarged using so-called 'tiled' scans [see Fig. 1(d)]. Here, instead of performing consecutive XCT scans at different heights, CT scans that partially overlap in the horizontal positions of the X-ray detector screen are acquired. To illustrate the detector tiling principle, a large object was imaged using this functionality. The sample consists of an equestrian saddle [see Fig. 4(a)] with outer dimensions of 60 cm wide and 45 cm high (larger than the detector FOV). Because of suspicion of defects in the saddle, it was subjected to X-ray inspection (experimental conditions: 150 kV, 100 W, SOD 1654mm, SDD 1996, 1 s exposure, 10 averages). In order to acquire the 4 tile images (3K mode, 2844×2856 pixels) [shown in Fig. 4(b)], the detector was translated from its central position horizontally by 213 mm and vertically by 80 mm. Even wider objects can be imaged as the translation of the detector (maximal range of 620 mm) allows almost 3 complete tiles within the maximal FOV. In this way, objects up to 85 cm wide and 110 cm high can be imaged. Being able to move the detector in X and Y direction independently from the source or object is imperative to achieve such composite images as sample movement or combined tube/detector movement would cause difficulties to adequately merge 2D images due to the cone-beam geometry of the X-ray beam. The resulting composite image in Figs. 4(c)–4(d) is a 5688×3935 pixel image with 124 µm pixel size. As the overview image revealed a confirmation of the suspected damage, the sample was moved towards the source (SOD 353 mm) to achieve a zoomed-in radiograph of that particular region with 27 µm pixel size (50 W tube power, 2 s exposure time and 10 averages).

3.2. *Helical scanning as an alternative for circular XCT/STAMINA to reduce cone beam artefacts*

As mentioned earlier, a way to enable high resolution CT scans of large objects with the FleXCT scanner is to perform several consecutive scans along the vertical axis using so-called STAMINA scans [see Fig. 1(b)]. A continuous variant of such scan can be obtained by performing a helical

Optics EXPRESS

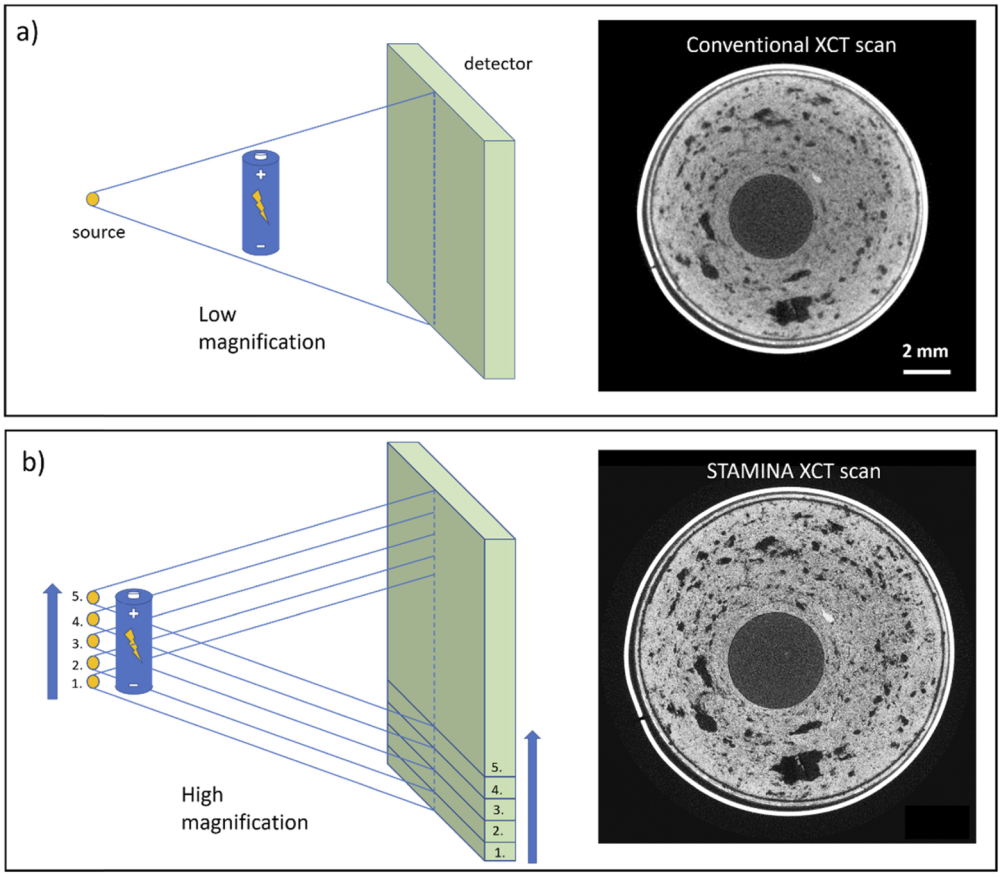

Fig. 3. Schematic representation (left) and reconstructed cross section (right) of a conventional XCT scan (a) and a STAMINA scan (b) of a conventional AA alkaline battery.

scan [see Fig. 1(c)]. To compare both methods, a circular and a helical scan were performed of a Li-ion battery (for more details on the experimental parameters, see Table 2). Source and detector panel were synchronously moved upward with a lateral speed of 0.17 mm/s, providing a 23.3 µm pitch, close to the 25 µm voxel size. Data was reconstructed using the FlexRayTools software package of which the results are shown in Fig. 5. The circular cone-beam scan (Fig. 5, left column) suffers from missing information, resulting in cone-beam artifacts increasingly present towards the top and bottom of the dataset. The helical trajectory, on the other hand, gathers information from a higher angular range in the vertical direction and fulfills Tuy's sampling condition. Helical reconstruction therefore overcomes the typical cone-beam artifacts that are clearly present at the top and bottom of the reconstructed circular cone-beam image. Additionally, for helical XCT, different rows of detector pixels are used to reconstruct a specific slice through the sample, which neutralizes detector effects, including ring artefacts. The use of non-circular orbits has been recently proposed for improving metal artifacts by Gang et al. [32], where metal artefacts were treated as missing information and Tuy's condition was used to determine the local data completeness metric. Helical scanning improved sampling and reduced missing data effects caused by metal implants.

Optics EXPRESS

Table 2. Overview of the different types of CT scans performed.[a]

sample	AA battery		Li ion battery		walnut	
scan type	CIRCULAR	STAMINA	CIRCULAR	HELICAL	CIRCULAR	CONVEYOR BELT
no. of discrete scans	1	5	1	1	1	1
energy (keV)	180	180	200	200	100	100
power (W)	40	15	30	30	30	30
filter	1.5 mm Cu	1.5 mm Cu	1mm Al	1mm Al	1 mm Al	1 mm Al
SOD (mm)	220	55	108	108	108	108
SDD (mm)	1000	1000	650	650	650	650
magnification	4.5	18	6	6	6	6
detector mode	HW1SW1LOW; 2K	HW1SW1LOW; 2K	HW1SW1LOW; 2K	HW1SW1LOW; 2K	HW1SW1LOW; 2K	HW1SW1LOW; 2K
exposure time (ms)	500	1200	140	140	75	75
no of averages	1	2	1	1	1	1
no of frames	2878	2878	2878	3579	2878	1022
voxel size (µm)	33	8.3	25	25	25	25
pitch (µm)	NA	NA	NA	23.3	NA	500
scan speed	0.25 deg/s	0.052 deg/s	0.894 deg/s (rot.)	0.893 deg/s (rot.) 0.167 mm/s (vert.)	1.67 deg/s (rot.)	6.67 mm/s (vert.)
datasize (Gb)	0.97	43.6	1.86 Gb	24.2 Gb	19.5	6.9 Gb
scan duration	27 min	9 h40	8 min	8 min	4 min	2 min

[a]Datasize reflects the size of the uncropped reconstructed slices. All tomographic data is available in TomoBank, a tomographic data repository for computational X-ray science [31]

3.3. *Conveyor belt type scanning for fast inspection*

For acquiring detailed XCT scans of samples that are larger than the field-of-view of the detector, STAMINA, tiled, and helical scans can be performed. Disadvantage of these scanning techniques is that they are rather slow because of the large number of projections that need to be acquired. Conveyor belt type scanning allows fast inspection with the object continuously moving in one direction without the need of rotation. Thanks to the multitude of degrees of freedom of motion with the FleXCT scanner, conveyor belt type scanning can be carried out in several ways: a) by moving either source and detector in horizontal/vertical direction or b) by moving the sample stage horizontally through the cone beam. Since the horizontal translation range of the sample stage is significantly smaller than the combined vertical travel range of X-ray tube and detector (470 mm and of 900 mm, respectively, see also Table 1), a conveyor belt geometry in vertical direction is the preferred method for larger samples.

To create a representative sample for conveyor belt scanning (i.e., sufficiently long, similar view), a total of 10 walnuts were stacked in a PVC tube with paper tissues put in between as spacers. Walnuts serve as an example for in-line inspection of food materials, or any other object undergoing quality control (e.g., additive manufactured parts). Recently, walnuts have been coined as datasets for machine learning applications given their natural inter-population variability [33]. To optimize the scanner settings, a single walnut was scanned in circular mode at 100 kV with 1 mm Al filter, and a 25 µm voxel size. An optimal exposure time of 75 ms/radiograph resulted in a scan duration of approx. 4 min (see Table 2). A schematic depiction of the conveyor

Optics EXPRESS

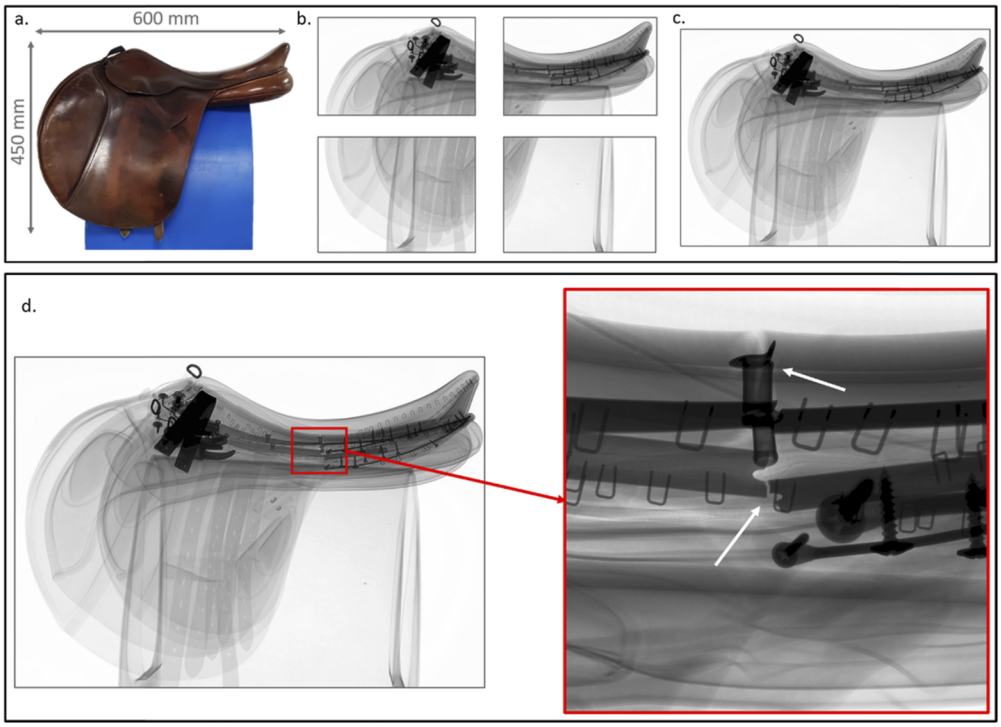

Fig. 4. Tiled imaging of an equestrian saddle: a) saddle mounted on a sample support for scanning, b) 4 composite images acquired by vertical and horizontal detector translation, c) composite image, d) detailed zoom-in radiography of damaged region.

belt type scan is provided in Fig. 6. Experimental conditions were set similar as compared to the conventional circular upon the single walnut. The conveyor belt type scan consisted of a vertical upward movement of source and detector along the sample at a speed of 6.67 mm/s, providing a pitch of 500 micron and a total of 1022 radiographs, sampling a total distance of approx. 50 cm, scanning all 10 walnuts in approx. 2 min. A movie of the entire radiograph sequence is provided in Visualization 2. To complement the conveyor belt data with a larger angular range, the same conveyor belt scan was repeated at 0, 20, 45, 65, 90, 110, 135, and 155° (8 angles in total).

A vertical line scan (also referred to as conveyor belt geometry) of a single walnut (2nd from bottom in Visualization 2) was reconstructed using the FlexRayTools software package to evaluate the overall quality of the scan. First, a vertical line scan from a *single angle* was reconstructed, i.e., a series of 2D radiographs, each with only a 500 µm movement in the vertical direction. The upper left image in Fig. 7 represents a reconstructed cross section through the walnut at the central YZ plane using such conveyor belt data at zero degree rotation position of the walnut only. It is important to note that the central YZ plane through the walnut (plane parallel to the detector, see Fig. 6) is probed under a larger angular range compared to the XY plane. Therefore, the first contains more detail compared to the plane perpendicular to the detector (XY) and is also referred to as the 'tomosynthesis' plane (see also Introduction for more information). Although representing information from one specific cross-section, the upper left tomosynthesis image in Fig. 7 apparently gives, as it were, added 3D information of the walnut sample. Note also that the tissue paper, used as a spacer between the walnuts located in the tube, can clearly be discerned. Second, vertical line scans obtained at *all 8 different rotation angles* (0, 20, 45, 65, 90, 110, 135, and 155°) were used as input for the reconstruction and are provided in the second

Optics EXPRESS

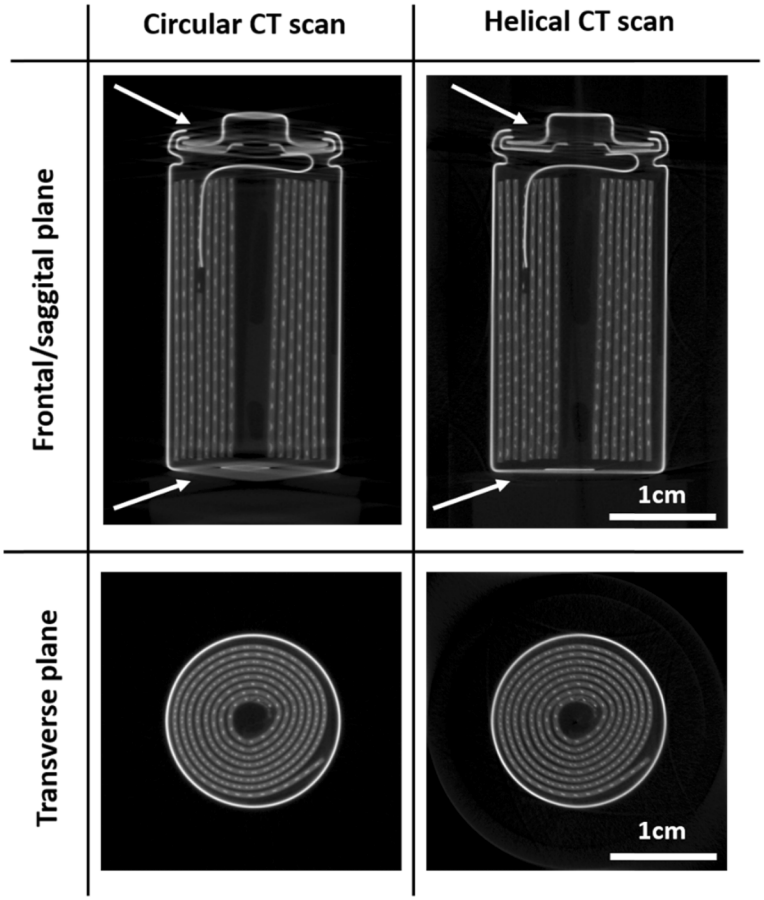

Fig. 5. Comparison of conventional and helical CT scan on battery sample.

column of Fig. 7. Logically, the reconstruction based on the (YZ) tomosynthesis planes (top right image in Fig. 7) provides a cross-section with less artifacts compared to the reconstruction of the XY planes (bottom right image in Fig. 7). Image sequences of the entire reconstructed image stacks in XZ, YZ and XZ orientation corresponding to Fig. 7 are provided in Visualization 3, Visualization 4, Visualization 5, Visualization 6, Visualization 7 and Visualization 8; image sequence of the tomosynthesis (YZ) planes for all 8 angles is provided in Visualization 9.

Next, radiography and tomosynthesis reconstructions of the entire line scan of all 10 walnuts were compared, of which the results are shown in Fig. 8. The radiographic image in Fig. 8 was obtained by extracting the central pixel row from the entire sequence of acquired radiographs. Below the (split up) radiographs, the corresponding tomosynthesis slice (YZ plane) is shown. Note that here, data from virtual slices through the notes is obtained instead of integrated radiography data. This is, for example, clearly visible in note no. 6, where the separation between the two nut halves is no longer visible centrally. Obtaining such 'true' fast inside/CT information compared to radiography alone can be of great importance for inline inspection of objects.

3.4. Four-dimensional (4D) XCT scanning

The FleXCT scanner also allows XCT analysis of samples changing through time through the acquisition of successive (continuous) full rotation scans. Since dynamic processes require fast

Optics EXPRESS

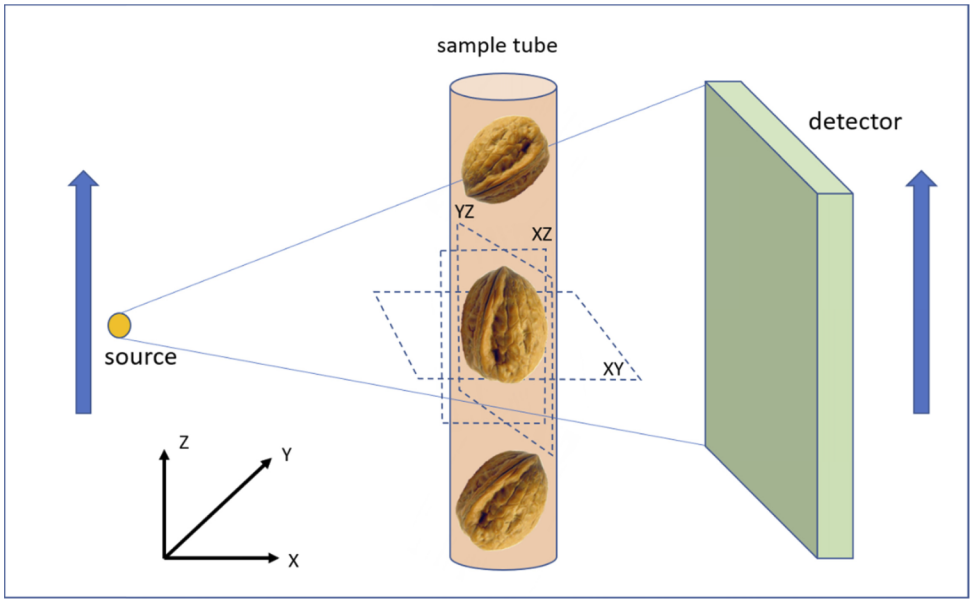

Fig. 6. Scanning scheme for a conveyor belt scan of 10 stacked walnuts stacked in a tube.

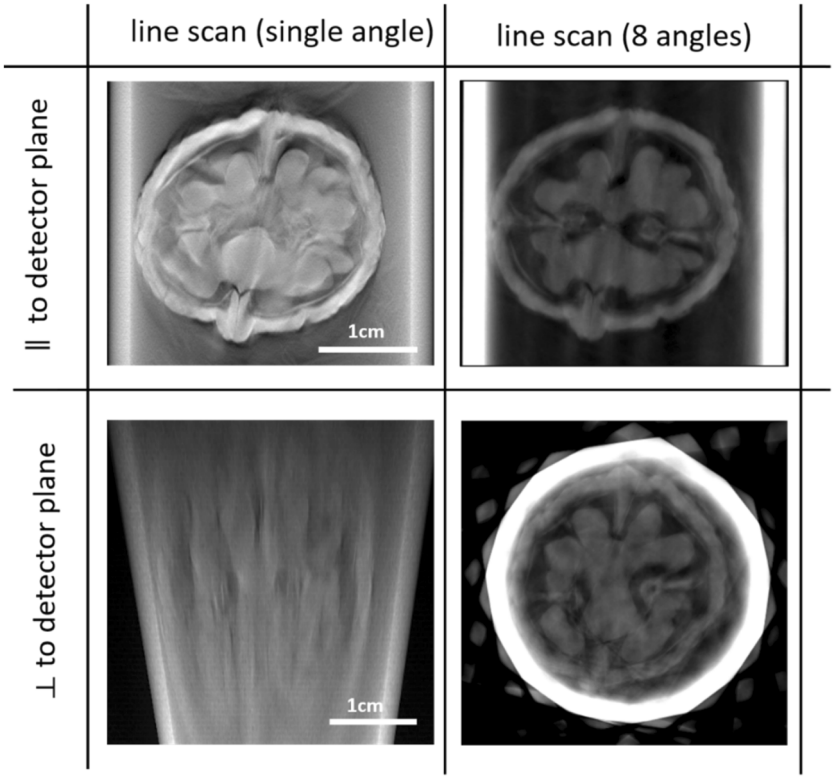

Fig. 7. CT reconstruction of a single walnut from a single conveyor belt line scan and conveyor belt scan repeated at 8 different angles (0, 20, 45, 65, 90, 110, 135, and 155°). First row: single walnut slice in parallel to the detector (YZ plane shown in Fig. 6), second row: walnut slice orthogonal to the detector (XY plane shown in Fig. 6).

Optics EXPRESS

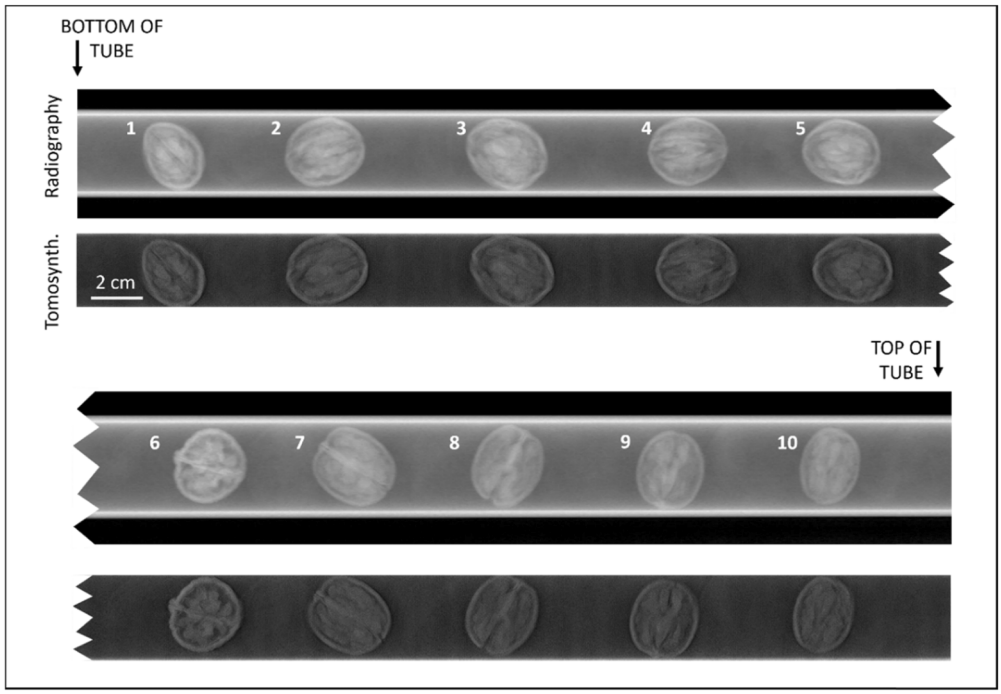

Fig. 8. Comparison of 2D radiography and tomosynthesis (YZ plane) of the entire stack of 10 walnuts.

imaging, the resulting radiographs are generally of lower signal-to-noise ratio (SNR) compared to radiographs from standard cone-beam CT. In order to improve SNR, 4D CT scans are taken at shorter SDD (typically <650 mm) and in a binned pixel mode, with the drawback of lower spatial resolution and increased cone beam artefacts. Additionally, the power of the tube is increased to the corresponding achievable resolution for that geometry (e.g., 50 W for a 50 µm voxel size).

Reconstruction of the 4DCT dataset is achieved by batch processing of the consecutive XCT scans. To illustrate 4DCT scanning, a simple dynamic system of foam bubbles collapsing, contained within a small plastic eppendorf tube was scanned [see photograph insert in Fig. 9(a)]. To this end, a few mL of water were placed in a classic 1.5 mL eppendorf vial, a drop of detergent was added, and the recipient was shaken briefly. All scanning parameters for the 4DCT scan such as X-ray tube energy, detector exposure time, pixel binning, SOD/SDD were optimized before shaking and mounting of the Eppendorf tube onto the sample stage. The 4DCT experiment was performed at 40 kV, without the use of a filter. To sample as fast as possible, the binning mode was set to 3, resulting in an acquisition time of only 16 ms per radiograph, showing still sufficient SNR. A total of 9 full rotations was registered, using 600 frames per rotation. To ensure optimal sampling, all data was acquired in continuous rotation mode. In this way, the scan can be performed in less than 2 minutes (excluding acquisition of flat/dark field images). In order to reach sufficient flux at the short exposure time used, the sample was positioned such that 100 µm spatial resolution was achieved, which enabled increasing the X-ray tube power up to 100 W. Figure 9(a) shows the two heights (h_1, h_2) of the Eppendorf tube for which the reconstructed cross-sections after the second full rotation (t=19.2s) were obtained [Fig. 9(b) and Fig. 9(c)]. The corresponding image sequence (n=9) of the 4DCT scan at these both heights is provided as image tiff stack in Visualization 10–Visualization 11, in which subtle movements and merging of foam bubbles can be observed.

Optics EXPRESS

3.5. Phase contrast XCT imaging

By changing the object-detector distance, enhanced phase contrast radiography/XCT can be obtained. To illustrate the phase imaging capability of the instrument, radiography experiments were performed upon an 8 mm diameter cylinder made from beryllium (Be), a material known for its high X-ray refraction (δ=0.212 at 25 kV, https://henke.lbl.gov/optical_constants/). The sample was placed at 193 mm from the source, after which the detector panel was put at maximal distance from the X-ray source (SDD 1995 mm), providing an effective pixel size of 5 µm. Radiographs were acquired at 25 kV (no filter), with optimal saturation of the detector (1000 ms exposure time, 10 averages), of which the results are shown in Fig. 10(a). To visualize the phase effect in more detail, an integrated line profile across the edge of the Be cylinder [indicated with a yellow rectangle in Fig. 10(a) is plotted in Fig. 10(b)]. At the sample edge, an increase of approximately 2.5% in pixel intensity can be observed compared to the air background, which clearly illustrates the occurrence of phase effects.

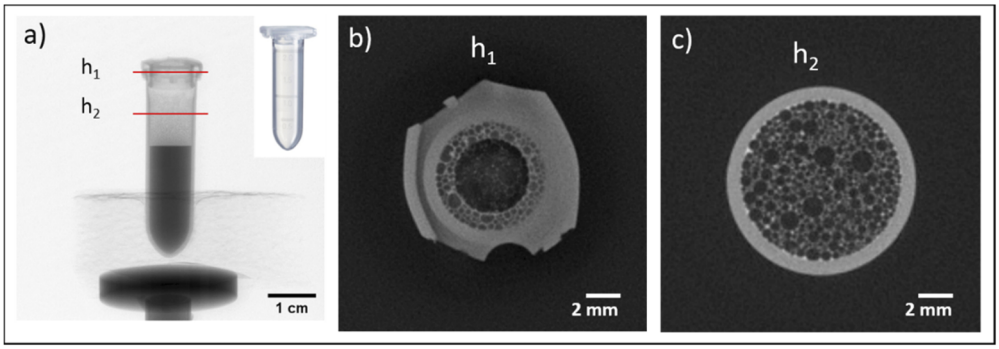

Fig. 9. 4DCT imaging of a briefly shaken Eppendorf tube containing soap water. Experimental conditions: 40 kV, 10 rotations, 600 frames/rotation, 16 ms exposure/frame and 100 µm voxel size. a) radiography of the Eppendorf tube (inset: photograph), b) reconstructed cross-section at height h_1 at t=19.2 s, c) identical, for height h_2. Image sequences for Fig. 8(b) and Fig. 8(c) from 0 s to 76.8 s (containing 9 frames) are provided in Visualization 10–Visualization 11.

Next, a plexiglass cylinder with 40 mm diameter (Röhm Gmbh, Germany) was measured at different SDD distances (SDD = 600, 1000, 1500 and 1995 mm) while keeping the voxel size constant at 25 µm [SDD 600 mm for Fig. 10(c)]. The cylinder was measured at 60 kV (no filter) with exposure time varying from 150 ms to 1500 ms with increasing SOD distance for optimal exposure of the detector. To visualize the effect of phase enhancement with increasing SDD distance, an integrated line profile is provided in Fig. 10(d), showing an increasing edge enhancement (phase) effect with increasing SDD distance (line profiles were shifted for clarity) [34].

To illustrate phase contrast imaging, radiography (and a CT scan) was performed upon a pumice stone [see Fig. 10(e)]. Instrument parameters were set at 100 kV, 1.5 mm Al filter, 60 µm voxel size and 5 averages/frame, for which a resulting normalized radiograph is shown on the left side of Fig. 10(e) (raw image). In the Acquila software package, phase-corrected absorption images was performed using the paganin method [14,35]. A phase corrected absorption contrast image is shown in Fig. 10(e) (right side, corrected).

In order to enable dedicated phase imaging in the future, the FleXCT scanner will be equipped with motorized absorption masks at the level of the sample and detector. By misalignment of both, refractive effects can be registered by the detector using a relatively new technique referred to as edge illumination (EI) [36]. Compared to grating based interferometry (GBI), which was

Optics EXPRESS

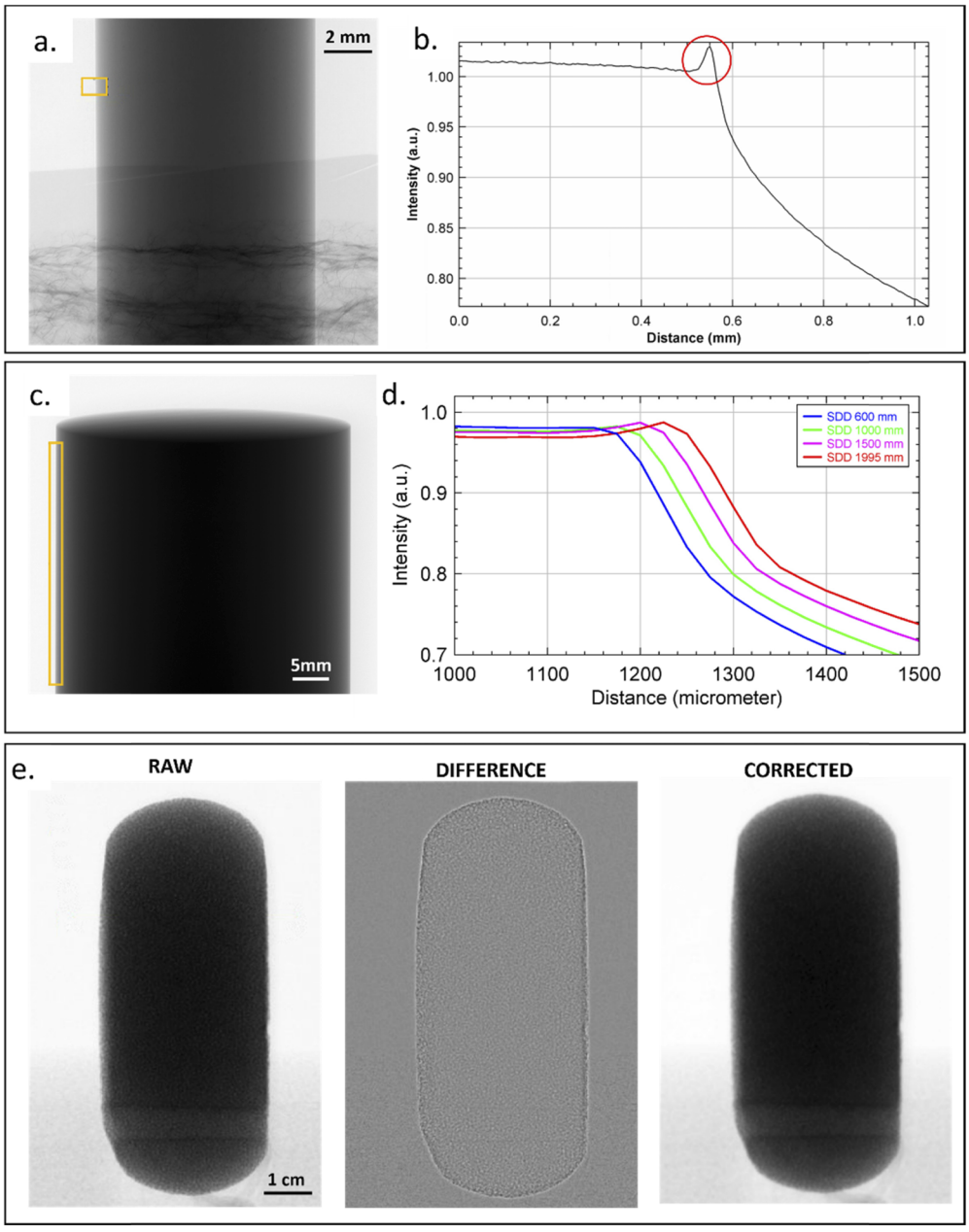

Fig. 10. a) radiograph of an 8 mm diameter beryllium rod, b) plot profile of the integrated line area across the rod edge, c) radiograph of a 40 mm plexi cylinder, d) plot profile of the integrated line area across the rod edge (line profiles were shifted for clarity), e) normalized radiograph of a pumice stone (left), difference image obtained for phase removal (middle), phase corrected absorption image using Paganin reconstruction filter.

Optics EXPRESS

first illustrated in a laboratory setting by Pfeiffer et al. [37], EI is less sensitive to incoherent X-rays and mechanical instabilities. In addition to phase imaging, EI (and GBI) allow to obtain an absorption and a dark-field image from the measured data. The latter represents scattering occurring at ultra-small angles, for example caused by small particles, pores and fibers [38]. These three complementary imaging modalities (absorption, phase, dark-field) allow for a more in-depth material analysis [39–41].

3.6. Other types on non-standard scanning

Besides the illustrated scanning geometries (e.g. tiled, stamina, helical, conveyor belt), additional, non-standard XCT geometries presented in Fig. 1 can be explored with the FleXCT scanner, such as dynamic zooming CT, laminography, limited wedge imaging, or a combination thereof. This is however outside the scope of this work, which aims to show the general, overall versatility of the FleXCT scanner in terms of scanning schemes and illustrate the reconstruction of a few showcase non-standard XCT scans with the FlexrayTools software package.

4. Conclusion and outlook

In this work, we highlighted the possibilities of a new, versatile X-ray CT scanner (FleXCT) that has been customised by Tescan XRE to study a wide variety of X-ray imaging scenarios. Due to its relatively large energy range (20–230 kV), large motor travel distances (e.g., up to 2 m source-detector distance) and a total of 10 motorized axes, a multitude of non-standard XCT scans is possible. We illustrated the recording of CT scans of larger objects at a resolution higher than achievable in conventional scans by means of stacked (or helical) scanning. The large number of motorized axes additionally enables conveyor belt type scanning for fast industrial analyses, adaptive zooming for asymmetrical objects, and laminography-based scans for samples too large to rotate or combinations of the foregoing techniques (e.g., rotation and conveyor belt). To enable users of the FleXCT scanner to perform experiments with those alternative geometries, we developed a software package 'FlexRayTools'. Tailor-made iterative reconstructions procedures form the backbone of the software package that enables efficient and fast reconstruction of non-standard/limited angle scanning geometries acquired with the FleXCT scanner instrument. Moreover, the FleXCT system is well suited to investigate fast-changing, dynamic systems (e.g. foam tracking, crack propagation) via 4DCT scanning. By increasing the source-detector distance, enhanced phase contrast imaging can be obtained using phase retrieval algorithms (Paganin, Bronnikov). In the future, the FleXCT scanner will be equipped with motorized absorption masks at the level of the sample and detector, providing multi-modal absorption, phase and dark-field imaging.

Funding. Austrian Science Fund (I 3261-N36); Agentschap Innoveren en Ondernemen (HBC.2019.2514); Fonds Wetenschappelijk Onderzoek (11D8319N, 1SA2920N, G0F9117N, I002718N, S004217N, S003421N, G094320N, G090020N).

Acknowledgments. We thank Jan Dewanckele, Manuel Dierick and Denis Van Loo (Tescan XRE) for valuable discussions, instrument assistance, and providing the horse saddle sample.

Disclosures. The authors declare that there are no conflicts of interest related to this article.

References

1. B. Masschaele, M. Dierick, D. Van Loo, M. N. Boone, L. Brabant, E. Pauwels, V. Cnudde, and L. Van Hoorebeke, "HECTOR: A 240 kV micro-CT setup optimized for research," in *11th International Conference on X-Ray Microscopy*, H. Xu, Z. Wu, and R. Tai, eds. (2013).
2. S. B. Coban, F. Lucka, W. J. Palenstijn, D. Van Loo, and K. J. Batenburg, "Explorative Imaging and Its Implementation at the FleX-ray Laboratory," J. Imaging **6**(4), 18 (2020).
3. H. Banjak, "X-ray Computed Tomography Reconstruction on Non-Standard Trajectories for Robotized Inspection, PhD thesis," (2016).
4. C. Vienne, M. Costin, "Adapted acquisition trajectory and iterative reconstruction for few-views CT inspection," *8th Conference on Industrial Computed Tomography (iCT) 2018-2*(2018).

Optics EXPRESS

5. www.tescan.com.
6. W. van Aarle, W. J. Palenstijn, J. Cant, E. Janssens, F. Bleichrodt, A. Dabravolski, J. De Beenhouwer, K. J. Batenburg, and J. Sijbers, "Fast and flexible X-ray tomography using the ASTRA toolbox," Opt. Express **24**(22), 25129–25147 (2016).
7. J. B. Thibault, K. D. Sauer, C. A. Bouman, and J. Hsieh, "A three-dimensional statistical approach to improved image quality for multislice helical CT," Med. Phys. **34**(11), 4526–4544 (2007).
8. H. Hu, "Multi-slice helical CT: Scan and reconstruction," Med. Phys. **26**(1), 5–18 (1999).
9. A. Dabravolski, "Towards In Loco X-ray Computed Tomography," PhD thesis (2015).
10. A. Dabravolski, K. J. Batenburg, and J. Sijbers, "Adaptive zooming in X-ray computed tomography," J. X-Ray Sci. Technol. **22**(1), 77–89 (2014).
11. G. Zang, R. Idoughi, R. Tao, G. Lubineau, P. Wonka, and W. Heidrich, "Space-time Tomography for Continuously Deforming Objects," ACM Transactions on Graphics **37**(4), 1–14 (2018).
12. J. D. Grunwaldt and C. G. Schroer, "Hard and soft X-ray microscopy and tomography in catalysis: bridging the different time and length scales," Chem. Soc. Rev. **39**(12), 4741–4753 (2010).
13. A. V. Bronnikov, "Developments in X-ray Tomography V. Edited by Bonse, Ulrich," Proceedings of the SPIE **6318**, 63180Q (2006).
14. D. Paganin, S. C. Mayo, T. E. Gureyev, P. R. Miller, and S. W. Wilkins, "Simultaneous phase and amplitude extraction from a single defocused image of a homogeneous object," J. Microsc. **206**(1), 33–40 (2002).
15. T. Weitkamp, D. Haas, D. Wegrzynek, and A. Rack, "ANKAphase: software for single-distance phase retrieval from inline X-ray phase-contrast radiographs," J. Synchrotron Radiat. **18**(4), 617–629 (2011).
16. E. Niemi, A. Salosensaari, A. Meaney, H. Lohman, and S. Siltanen, "Limited-angle X-ray tomography for weld inspection," in 2018).
17. M. H. Krumm, H. Cárdenez, and C. Sauerwein, "3D X-ray Inspection System for Helicopter Rotor Blades," *11th International Symposium "NDT in Aerospace"*, 1–5 (2019).
18. J. T. Dobbins and D. J. Godfrey, "Digital x-ray tomosynthesis: current state of the art and clinical potential," Phys. Med. Biol. **48**(19), R65–R106 (2003).
19. L. F. A. Pereira, A. Dabravolski, T. I. Ren, G. D. C. Cavalcanti, and J. Sijbers, Conveyor belt X-ray CT using Domain Constrained Discrete Tomography, *2014 27th Sibgrapi Conference on Graphics, Patterns and Images* (Ieee, New York, 2014), pp. 290–297. DOI: 10.1109/sibgrapi.2014.21
20. F. Xu, L. Helfen, T. Baumbach, and H. Suhonen, "Comparison of image quality in computed laminography and tomography," Opt. Express **20**(2), 794–806 (2012).
21. A. Marinovszki, J. De Beenhouwer, and J. Sijbers, "An efficient CAD projector for X-ray projection based 3D inspection with the ASTRA Toolbox," NDT.net (2018).
22. H. Miao, H. Zhao, F. Gao, and S. Gong, "Implementation of FDK Reconstruction Algorithm in Cone-Beam CT Based on the 3D Shepp-Logan Model," in *2009 2nd International Conference on Biomedical Engineering and Informatics*, 2009), 1–5.
23. L. F. A. Pereira, J. De Beenhouwer, J. Kastner, and J. Sijbers, "Extreme Sparse X-ray Computed Laminography Via Convolutional Neural Networks," *32th International Conference on Tools with Artificial Intelligence* (2020).
24. X. G. Yang, M. Kahnt, D. Bruckner, A. Schropp, Y. Fam, J. Becher, J. D. Grunwaldt, T. L. Sheppard, and C. G. Schroer, "Tomograohic reconstruction with a generative adversarial network," J. Synchrot. Radiat. **27**, 486–493 (2020).
25. A. Kostenko, W. J. Palenstijn, S. B. Coban, A. A. Hendriksen, R. van Liere, and K. J. Batenburg, "Prototyping X-ray tomographic reconstruction pipelines with FleXbox," SoftwareX **11**, 100364 (2020).
26. P. R. Granfors and D. Albagli, "Scintillator-based flat-panel x-ray imaging detectors," J. Soc. Inf. Disp. **17**(6), 535–542 (2009).
27. M. Dierick, D. Van Loo, B. Masschaele, M. Boone, and L. Van Hoorebeke, "A LabVIEW (R) based generic CT scanner control software platform," J. X-Ray Sci. Technol. **18**(4), 451–461 (2010).
28. W. van Aarle, W. J. Palenstijn, J. De Beenhouwer, T. Altantzis, S. Bals, K. J. Batenburg, and J. Sijbers, "The ASTRA Toolbox: A platform for advanced algorithm development in electron tomography," Ultramicroscopy **157**, 35–47 (2015).
29. D. M. Pelt, D. Gursoy, W. J. Palenstijn, J. Sijbers, F. De Carlo, and K. J. Batenburg, "Integration of TomoPy and the ASTRA toolbox for advanced processing and reconstruction of tomographic synchrotron data," J. Synchrotron Radiat. **23**(3), 842–849 (2016).
30. W. J. Palenstijn, J. Bedorf, J. Sijbers, and K. J. Batenburg, "A distributed ASTRA toolbox," Adv. Struct. Chem. Imaging **2**(1), 19 (2016).
31. F. De Carlo, D. Gursoy, D. J. Ching, K. J. Batenburg, W. Ludwig, L. Mancini, F. Marone, R. Mokso, D. M. Pelt, J. Sijbers, and M. Rivers, "TomoBank: a tomographic data repository for computational x-ray science," Meas. Sci. Technol. **29**(3), 034004 (2018).
32. G. J. Gang, T. Russ, Y. Ma, C. Toennes, J. H. Siewerdsen, L. R. Schad, and J. W. Stayman, "Metal-Tolerant Noncircular Orbit Design and Implementation on Robotic C-Arm Systems," *The 6th International Conference on Image Formation in X-Ray Computed Tomography*, 400–403 (2020).
33. H. D. Sarkissian, F. Lucka, M. van Eijnatten, G. Colacicco, S. B. Coban, and K. J. Batenburg, "A cone-beam X-ray computed tomography data collection designed for machine learning," Sci. Data **6**(1), 8 (2019).

Optics EXPRESS

34. M. Endrizzi, "X-ray phase-contrast imaging," Nucl. Instrum. Methods Phys. Res., Sect. A **878**, 88–98 (2018).
35. A. Burvall, U. Lundstrom, P. A. C. Takman, D. H. Larsson, and H. M. Hertz, "Phase retrieval in X-ray phase-contrast imaging suitable for tomography," Opt. Express **19**(11), 10359–10376 (2011).
36. A. Olivo and R. Speller, "A coded-aperture technique allowing x-ray phase contrast imaging with conventional sources," Appl. Phys. Lett. **91**(7), 074106 (2007).
37. F. Pfeiffer, T. Weitkamp, O. Bunk, and C. David, "Phase retrieval and differential phase-contrast imaging with low-brilliance X-ray sources," Nat. Phys. **2**(4), 258–261 (2006).
38. M. von Teuffenbach, T. Koehler, A. Fehringer, M. Viermetz, B. Brendel, J. Herzen, R. Proksa, E. J. Rummeny, F. Pfeiffer, and P. B. Noel, "Grating-based phase-contrast and dark-field computed tomography: a single-shot method," Sci. Rep. **7**(1), 8 (2017).
39. P. Modregger, T. P. Cremona, C. Benarafa, J. C. Schittny, A. Olivo, and M. Endrizzi, "Small angle x-ray scattering with edge-illumination," Sci. Rep. **6**(1), 30940 (2016).
40. F. Schaff, F. Prade, Y. Sharma, M. Bech, and F. Pfeiffer, "Non-iterative Directional Dark-field Tomography," Sci Rep 7(1), 3307(2017).
41. T. Lauridsen, E. M. Lauridsen, and R. Feidenhans'l, "Mapping misoriented fibers using X-ray dark field tomography," Appl. Phys. A: Mater. Sci. Process. **115**(3), 741–745 (2014).